

Unfiltering of the Geostationary Earth Radiation Budget (GERB) Data. Part II: Longwave Radiation

N. CLERBAUX, S. DEWITTE, C. BERTRAND, D. CAPRION, B. DE PAEPE, L. GONZALEZ, AND A. IPE

Royal Meteorological Institute of Belgium, Brussels, Belgium

J. E. RUSSELL

Imperial College, London, United Kingdom

(Manuscript received 28 February 2007, in final form 4 September 2007)

ABSTRACT

The method used to estimate the unfiltered longwave broadband radiance from the filtered radiances measured by the Geostationary Earth Radiation Budget (GERB) instrument is presented. This unfiltering method is used to generate the first released edition of the GERB-2 dataset. This method involves a set of regressions between the unfiltering factor (i.e., the ratio of the unfiltered and filtered broadband radiances) and the narrowband observations of the Spinning Enhanced Visible and Infrared Imager (SEVIRI) instrument. The regressions are theoretically derived from a large database of simulated spectral radiance curves obtained by radiative transfer computations. The generation of this database is fully described.

Different sources of error that may affect the GERB unfiltering have been identified and the associated error magnitudes are assessed on the database. For most of the earth-atmosphere conditions, the error introduced during the unfiltering processes is well under 0.5% (RMS error of about 0.1%). For more confidence, the unfiltered radiances of GERB-2 are validated by cross comparison with collocated and coangular Clouds and the Earth's Radiant Energy System (CERES) observations. The agreement between the unfiltered radiances is within the science goals (1% accuracy for GERB and 0.5% for CERES) for the Flight Model 2 (FM2). For the CERES Flight Model 3 (FM3) instrument, an overall difference of 1.8% is observed. The intercomparisons indicate some scene-type dependency, which is due to the unfiltering for the cloudy scenes. This should be corrected for subsequent editions of the database.

1. Introduction

This paper describes the methodology used to determine the unfiltered longwave radiance from the filtered radiances of the Geostationary Earth Radiation Budget (GERB)-2 instrument on the *Meteosat Second Generation (MSG)-1*. The unfiltering of the shortwave channel is described in Clerbaux et al. (2008, hereafter Part I), which is presumed to be known by the reader.

As previous broadband instruments like the Clouds and the Earth's Radiant Energy System (CERES; Wielicki et al. 1996) or the Scanner for Radiation Budget (ScaRaB), the GERB longwave (LW) radiance is

obtained as the difference between a total (TOT) and a shortwave (SW) measurement. However, for GERB, some difficulties arise from the fact that those measurements may differ significantly in time (up to 170 s) and location. Dewitte et al. (2008) describe how this is handled by the data processing. The GERB instrument contains a linear array of 256 detector elements, and this is also challenging as each detector has its own spectral sensitivity. On the other hand, the unfiltering can make use of abundant spectral information provided by seven narrowband (NB) infrared measurements of the Spinning Enhanced Visible and Infrared Imager (SEVIRI; Schmetz et al. 2002), the operational weather imager on board the MSG satellite series.

The paper is structured as follows. First, the spectral response curve of the GERB-2 longwave channel is presented. Section 3 states the unfiltering problem as well as some operational constraints for the implementation of this part of the GERB data processing. Section

Corresponding author address: Nicolas Clerbaux, Royal Meteorological Institute of Belgium, Ringlaan 3 Avenue Circulaire B-1180, Brussels, Belgium.
E-mail: nicolas.clerbaux@oma.be

4 presents the radiative transfer computations that are used to parameterize the unfiltering. A comprehensive description of the unfiltering is provided in section 5. This includes the details of the method and the parameters derived for the GERB-2 instrument. Based on radiative transfer computations, the theoretical errors introduced by the unfiltering processes are assessed in section 6. Section 7 presents the results of an intercomparison of GERB-2 and CERES Flight Model 2 (FM2) and 3 (FM3) unfiltered radiance. This intercomparison is an overall validation of the GERB unfiltered radiance, which includes the effects of the characterization of the instrument spectral response as well as the errors introduced during the unfiltering. A final discussion of the GERB longwave channel unfiltering is provided in section 8.

2. The GERB longwave spectral response

Successive GERB scans measure the total radiation (TOT channel) and the shortwave radiation (Harries et al. 2005). The shortwave measurement is realized through a quartz filter, which only transmits wavelengths shorter than about 4.0 μm , while the total measurement is realized without the filter. The longwave (synthetic) channel is defined as the subtraction

$$\phi_{\text{lw}}^{\text{det}}(\lambda) = \phi_{\text{tot}}^{\text{det}}(\lambda) - A^{\text{det}} \phi_{\text{sw}}^{\text{det}}(\lambda), \quad (1)$$

with the A^{det} factor set for each detector in such a way that the LW radiance is zero for a Planck's spectrum at 5800 K:

$$A^{\text{det}} = \frac{\int \phi_{\text{tot}}^{\text{det}}(\lambda) L_{5800\text{K}}(\lambda) d\lambda}{\int \phi_{\text{sw}}^{\text{det}}(\lambda) L_{5800\text{K}}(\lambda) d\lambda}. \quad (2)$$

Figure 1 shows the synthetic longwave spectral response curve $\phi_{\text{lw}}(\lambda)$ determined from the measured GERB SW and TOT responses using Eqs. (1) and (2). Although individual curve exists for each detector, the figure only shows the average over the 256 detector elements of the GERB-2 instrument:

$$\phi_{\text{lw}}(\lambda) = \frac{1}{256} \sum_{\text{det}=1}^{256} \phi_{\text{lw}}^{\text{det}}(\lambda). \quad (3)$$

This curve is the system-level spectral response that gathers the responses of the detector, the quartz filter, the three mirrors of the reflective telescope, and the de-spin and depolarization mirrors.

The longwave channel presents its highest sensitivity between 5 and 50 μm . This sensitivity is more or less

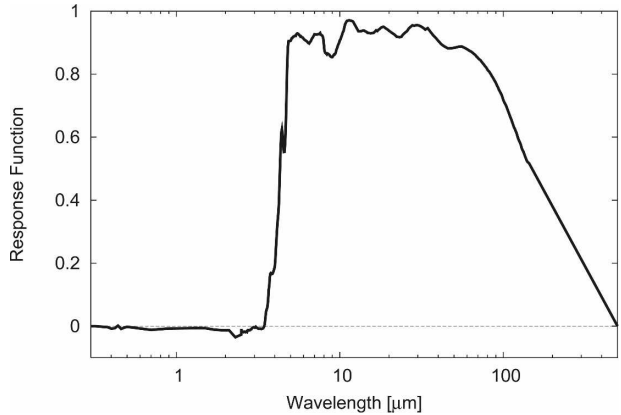


FIG. 1. LW average spectral response for the GERB-2 instrument.

constant, although the minimum is observed near $\lambda \sim 9 \mu\text{m}$ ($\phi_{\text{lw}} \sim 0.85$) and the maximum near $\lambda \sim 11.5 \mu\text{m}$ ($\phi_{\text{lw}} \sim 0.97$). These variations are due to the five mirrors of the instrument's optics.

3. Problem statement and constraints

To be scientifically useful, the filtered radiances L_{tot} and L_{sw} measured by the instrument must be converted to unfiltered emitted thermal radiance L_{th} , the radiance that would have been measured by a perfect broadband instrument [i.e., $\phi_{\text{lw}}(\lambda) = 1, \forall \lambda$] sensitive only to the infrared radiation that is emitted by our planet:

$$L_{\text{th}} = \int L_{\text{th}}(\lambda) d\lambda. \quad (4)$$

A spatial and temporal processing (Dewitte et al. 2008) is realized to interpolate the TOT measurements to the point spread function (PSF) and acquisition time of the SW measurements. The GERB synthetic filtered longwave radiance is then defined as

$$L_{\text{lw}} = L_{\text{tot}}^{\text{interpolated}} - A^{\text{det}} L_{\text{sw}}. \quad (5)$$

This longwave radiance L_{lw} consists mainly to emitted thermal radiation $L_{\text{lw,th}}$ but also includes a small contribution $L_{\text{lw,sol}}$ because of the reflected solar radiation:

$$\begin{aligned} L_{\text{lw}} &= L_{\text{lw,th}} + L_{\text{lw,sol}}, \\ &= \int L_{\text{th}}(\lambda) \phi_{\text{lw}}(\lambda) d\lambda + \int L_{\text{sol}}(\lambda) \phi_{\text{lw}}(\lambda) d\lambda. \end{aligned} \quad (6)$$

The sign of the solar contribution $L_{\text{lw,sol}}$ is, in general, negative because the $\phi_{\text{lw}}(\lambda)$ presents small negative values in the visible part of the spectrum (Fig. 1). This

comes from the definition of the synthetic longwave radiance that has zero radiance when a 5800-K blackbody is observed. The unfiltering factor for the LW channel is defined as the ratio

$$\alpha_{lw} = L_{th}/L_{lw,th}. \quad (7)$$

For the same reason as for the shortwave channel (Part I), the unfiltering is realized in two steps. In a first step, the NB infrared measurements of the SEVIRI imager are used to estimate the broadband unfiltered thermal radiance L'_{th} and the filtered longwave radiance L'_{lw} . In the second step, the two SEVIRI estimates are convolved with the GERB dynamic PSF and temporally interpolated to match the GERB measurements. The GERB unfiltered thermal radiance is finally obtained by multiplying the filtered radiance L_{lw} given by Eq. (5) by a factor equal to the ratio of the SEVIRI estimated unfiltered and filtered radiances:

$$L_{th} = L_{lw} \left(\frac{L'_{th}}{L'_{lw,th} + L'_{lw,sol}} \right) \left[= L'_{th} \left(\frac{L_{lw}}{L'_{lw,th} + L'_{lw,sol}} \right) \right]. \quad (8)$$

The advantages of this approach have been discussed in Part I. It must be recognized that the solar contamination $L'_{lw,sol}$ is not properly accounted for in Eq. (8). Indeed, it would have been more rigorous to estimate the unfiltered GERB radiance as

$$L_{th} = (L_{lw} - L'_{lw,sol}) \left(\frac{L'_{th}}{L'_{lw,th}} \right) \left[= L'_{th} \left(\frac{L_{lw} - L'_{lw,sol}}{L'_{lw,th}} \right) \right], \quad (9)$$

so that the result is not dependent on the absolute SEVIRI calibration that affects the L'_{th} and $L'_{lw,th}$ (calibration error cancels in the ratio). The unfiltering error introduced in the edition 1 GERB data due to the use of Eq. (8) instead of Eq. (9) is, however, very small and is quantified in section 6c.

4. Radiative transfer computations

A large database of simulated spectral radiance curves $L_{th}(\lambda)$ is built using version 1.21 of the Santa Barbara discrete ordinate radiative transfer (DISORT) Atmospheric Radiative Transfer (SBDART; Ricchiuzzi et al. 1998) model. The simulations are performed for 4622 realistic conditions of the earth-atmosphere system, as described in Clerbaux et al. (2003). The database is available from the Royal Meteorological Institute of Belgium (RMIB) GERB team Web site (<http://gerb.oma.be/SpectralRadiancesDB/>).

All the simulations are made with the incoming solar

radiation turned off to simulate only the radiation due to the planetary thermal emission $L_{th}(\lambda)$. The computations have been made at 431 wavelengths λ covering the thermal region 2.5–100 μm , which are the lower and upper limits for SBDART thermal simulation. Between 2.5 and 20 μm a wavelength increment of $\delta\lambda = 0.05 \mu\text{m}$ is used, while between 20 and 100 μm the increment is $\delta\lambda = 1.0 \mu\text{m}$, to limit the computation time. The spectral radiance curves $L(\lambda)$ are then extended up to 500 μm using Planck's law with the brightness temperature given by the radiative transfer model at 100 μm . For each wavelength and each simulation, the spectral radiance field is computed with a 5° resolution in viewing zenith angle ($\text{VZA} = 0^\circ, 5^\circ, 10^\circ, \dots, 85^\circ$). The DISORT computations are performed using 16 streams to obtain an accurate representation of the dependency of the scene spectral signature $L(\lambda)$ with the VZA.

The atmospheric profile is by far the primary input for the radiative transfer computations in the thermal part of the spectrum. For the simulations, the profiles compiled in the Thermodynamic Initial Guess Retrieval, version 3 (TIGR-3) database (Chevallier et al. 2000) have been used. These data have been kindly made available by the Laboratoire de Meteorologie Dynamique. The profiles provide, at 40 pressure levels (1013, 955, \dots , 0.05 hPa) the height, temperature, and concentrations in water vapor and ozone.

For each simulation, the surface skin temperature is set randomly and with a uniform distribution of probability between $T_0 - 15 \text{ K}$ and $T_0 + 15 \text{ K}$, where T_0 is the temperature at the lower atmospheric profile level. This aims to account for the radiative heating or cooling of the surface. However, in some daytime situations, much higher differences between the surface and air temperature are observed, as, for example, over clear desert at the beginning of the afternoon. To simulate this, for 40% of the simulations, the surface skin temperature is set randomly and with uniform distribution of probability between T_0 and $T_0 + 50 \text{ K}$. The surface emissivity ϵ must also be specified for the simulations. Ideally, this emissivity should be spectrally dependent $\epsilon(\lambda)$ but, unfortunately, realistic curves $\epsilon(\lambda)$ defined over the 2.5–100- μm interval are not yet available. Spectrally invariant emissivity is then used and set randomly with a uniform distribution of probability between 0.85 and 1.

Realistic cloud covers should also be simulated. This is done for half of the simulations; the other half is cloud free. The cloudiness can consist of up to three different overlapping cloud layers. The characteristics of these layers are each independent of the others. The lower cloud layer is simulated with a probability of 50%, is located at a height between 500 and 3500 m

(uniform distribution of probability), and is always constituted of water droplets. The probability of middle-level cloud is 40%, the layer is located between 4000 and 7000 m, and it is constituted of ice particles in 25% of the cases and water droplets in 75% of the cases. The probability of high-level cloud is 30%, the layer is located between 7000 and 16 000 m, and it is always constituted of ice particles. For a water phase layer, two kinds of clouds are simulated with an equal probability: precipitating and nonprecipitating clouds. The effective radius of the droplet size distribution is then chosen randomly and with a uniform distribution of probability within [2: 25] μm for nonprecipitating clouds and within [25: 128] μm for precipitating clouds. For an ice phase layer, the single-scattering coalbedo ($1 - a$) predicted using the Mie theory is modified by a multiplicative factor chosen randomly in the range [0.5: 1], as suggested by Ricchiazzi et al. (1998). The single-scattering coalbedo is the ratio between the probability of absorption and the probability of scattering. Finally, the optical thickness of the cloud layers must be specified. The thickness class is selected randomly with an equal probability between thin, medium, and thick layers. The optical thickness (at 0.55 μm) is then selected randomly within [0: 3.6] (thin), [3.6: 23] (medium), and [23: 379] (thick); in each case there is a uniform distribution of probability. These threshold values for cloud optical thickness and cloud height are adopted to match the International Satellite Cloud Climatology Project (ISCCP) cloud classification (Rossow and Schiffer 1991).

The type of boundary layer aerosol is chosen randomly and with an equal probability within the following types: none, rural, urban, oceanic, and tropospheric. The SBDART model default parameterization and wavelength dependency are used for this kind of aerosol. No stratospheric aerosols are added in the simulations.

This database of spectral radiance curves is then weighted with the instrument's spectral response filters to get the following broadband and narrowband radiances:

$$\begin{aligned}
 L_{\text{th}} &= \int_{2.5\mu\text{m}}^{500\mu\text{m}} L_{\text{th}}(\lambda) d\lambda, \\
 L_{1\text{w,th}} &= \int_{2.5\mu\text{m}}^{500\mu\text{m}} L_{\text{th}}(\lambda)\phi_{1\text{w}}(\lambda) d\lambda, \\
 L_{6.2} &= \int_{2.5\mu\text{m}}^{500\mu\text{m}} L_{\text{th}}(\lambda)\phi_{6.2}(\lambda) d\lambda, \\
 L_{7.3} &= \int_{2.5\mu\text{m}}^{500\mu\text{m}} L_{\text{th}}(\lambda)\phi_{7.3}(\lambda) d\lambda, \\
 L_{8.7} &= \int_{2.5\mu\text{m}}^{500\mu\text{m}} L_{\text{th}}(\lambda)\phi_{8.7}(\lambda) d\lambda, \\
 L_{9.7} &= \int_{2.5\mu\text{m}}^{500\mu\text{m}} L_{\text{th}}(\lambda)\phi_{9.7}(\lambda) d\lambda, \\
 L_{10.8} &= \int_{2.5\mu\text{m}}^{500\mu\text{m}} L_{\text{th}}(\lambda)\phi_{10.8}(\lambda) d\lambda, \\
 L_{12.0} &= \int_{2.5\mu\text{m}}^{500\mu\text{m}} L_{\text{th}}(\lambda)\phi_{12.0}(\lambda) d\lambda, \quad \text{and} \\
 L_{13.4} &= \int_{2.5\mu\text{m}}^{500\mu\text{m}} L_{\text{th}}(\lambda)\phi_{13.4}(\lambda) d\lambda, \quad (10)
 \end{aligned}$$

where $\phi_{1\text{w}}(\lambda)$ is the GERB-2 average longwave spectral response defined by Eq. (3), and $\phi_{6.2}(\lambda), \dots, \phi_{13.4}(\lambda)$ are the spectral responses of the thermal channels of the SEVIRI instrument on *MSG-1* [available from the European Organisation for the Exploitation of Meteorological Satellites (EUMETSAT)]. In practice, all the radiances are expressed in units of $\text{W m}^{-2} \text{sr}^{-1}$.

5. The edition 1 GERB LW unfiltering

a. Narrowband-to-broadband regressions

A set of theoretical regressions has been derived from the radiative transfer computations to estimate the broadband (BB) radiances L'_{th} and $L'_{1\text{w,th}}$ as a function of the SEVIRI thermal channel radiances. For this, second-order polynomial regressions have been adopted:

$$\begin{aligned}
 L'_{\text{th}} &= a_0 + a_1L_{6.2} + a_2L_{7.3} + a_3L_{8.7} + a_4L_{9.7} + a_5L_{10.8} + a_6L_{12} + a_7L_{13.4} + a_8L_{6.2}^2 + a_9L_{7.3}L_{6.2} + a_{10}L_{7.3}^2 \\
 &+ a_{11}L_{8.7}L_{6.2} + a_{12}L_{8.7}L_{7.3} + \dots + a_{35}L_{13.4}^2, \quad \text{and} \quad (11)
 \end{aligned}$$

$$\begin{aligned}
 L'_{1\text{w,th}} &= b_0 + b_1L_{6.2} + b_2L_{7.3} + b_3L_{8.7} + b_4L_{9.7} + b_5L_{10.8} + b_6L_{12} + b_7L_{13.4} + b_8L_{6.2}^2 + b_9L_{7.3}L_{6.2} + b_{10}L_{7.3}^2 \\
 &+ b_{11}L_{8.7}L_{6.2} + b_{12}L_{8.7}L_{7.3} + \dots + b_{35}L_{13.4}^2. \quad (12)
 \end{aligned}$$

TABLE 1. Regression parameters used to estimate the broadband unfiltered and filtered radiance from the seven thermal channels of SEVIRI. The parameters $\{a_i\}$ and $\{b_i\}$ are derived for VZA = 0°, 5°, 10°, . . . , 85°, but because of the limited space the table only provides values at VZA = 0°, 25°, 50°, and 75°, with a limited number of digits.

Coef	VZA = 0°	VZA = 25°	VZA = 50°	VZA = 75°
a_0/b_0	15.328/13.981	15.161/13.831	14.787/13.513	13.876/12.728
a_1/b_1	19.091/17.795	18.753/17.500	17.370/16.273	12.377/11.486
a_2/b_2	10.309/9.586	11.152/10.344	14.003/12.940	20.929/19.513
a_3/b_3	2.859/2.355	3.230/2.685	4.339/3.722	5.018/4.627
a_4/b_4	10.124/9.224	10.070/9.171	9.470/8.614	6.406/5.811
a_5/b_5	0.909/0.842	0.928/0.865	1.064/1.010	1.636/1.531
a_6/b_6	1.288/1.325	1.245/1.293	1.075/1.133	1.527/1.467
a_7/b_7	3.560/3.320	3.513/3.267	3.336/3.072	2.877/2.608
a_8/b_8	-4.453/-4.132	-4.784/-4.440	-6.276/-5.836	-15.022/-13.910
a_9/b_9	-1.787/-1.693	-2.250/-2.116	-3.054/-2.839	0.164/-0.046
a_{10}/b_{10}	2.756/2.516	2.997/2.744	3.132/2.886	-1.386/-1.110
a_{11}/b_{11}	1.501/1.563	1.145/1.291	0.034/0.446	-2.085/-1.605
a_{12}/b_{12}	1.976/1.659	2.322/1.927	3.216/2.623	4.911/4.499
a_{13}/b_{13}	0.882/0.530	0.916/0.517	0.968/0.446	1.013/0.613
a_{14}/b_{14}	0.364/0.459	0.841/0.897	1.834/1.746	4.326/3.847
a_{15}/b_{15}	-1.789/-1.731	-2.315/-2.216	-3.076/-2.889	-2.088/-1.949
a_{16}/b_{16}	-1.499/-1.443	-1.586/-1.514	-1.680/-1.564	-0.784/-0.638
a_{17}/b_{17}	3.626/3.385	3.749/3.501	3.767/3.505	0.432/0.416
a_{18}/b_{18}	-0.225/-0.239	-0.217/-0.235	-0.172/-0.207	0.285/0.220
a_{19}/b_{19}	-0.451/-0.394	-0.505/-0.441	-0.680/-0.594	-1.315/-1.220
a_{20}/b_{20}	-0.584/-0.567	-0.594/-0.563	-0.597/-0.526	-0.417/-0.392
a_{21}/b_{21}	-1.195/-1.125	-1.156/-1.091	-0.961/-0.913	-0.332/-0.324
a_{22}/b_{22}	0.185/0.176	0.181/0.172	0.165/0.154	0.075/0.074
a_{23}/b_{23}	0.553/0.463	0.655/0.542	1.085/0.902	1.762/1.612
a_{24}/b_{24}	-0.930/-0.832	-0.949/-0.835	-1.055/-0.906	-0.998/-0.971
a_{25}/b_{25}	0.431/0.613	0.435/0.646	0.411/0.692	-0.087/0.138
a_{26}/b_{26}	0.680/0.667	0.732/0.714	0.810/0.780	0.877/0.807
a_{27}/b_{27}	-0.068/-0.066	-0.079/-0.079	-0.109/-0.119	-0.074/-0.081
a_{28}/b_{28}	-0.084/-0.115	-0.088/-0.124	-0.090/-0.135	-0.018/-0.048
a_{29}/b_{29}	-1.480/-1.398	-1.333/-1.268	-0.855/-0.835	0.630/0.574
a_{30}/b_{30}	-0.413/-0.325	-0.559/-0.457	-0.961/-0.829	-1.157/-1.042
a_{31}/b_{31}	-0.560/-0.457	-0.657/-0.555	-0.906/-0.830	-0.831/-0.865
a_{32}/b_{32}	-0.724/-0.677	-0.745/-0.696	-0.792/-0.735	-0.485/-0.443
a_{33}/b_{33}	0.276/0.256	0.291/0.270	0.308/0.286	0.199/0.193
a_{34}/b_{34}	0.135/0.096	0.150/0.112	0.211/0.181	0.046/0.056
a_{35}/b_{35}	-0.108/-0.102	-0.105/-0.097	-0.097/-0.085	-0.070/-0.057
RMS error $\text{W m}^{-2} \text{sr}^{-1}$	0.464/0.428	0.461/0.425	0.447/0.412	0.386/0.356
Percent	0.655/0.655	0.658/0.658	0.660/0.660	0.623/0.624

The regression coefficients $\{a_i\}$ and $\{b_i\}$ are estimated as a best fit on the database of spectral radiance curves for each VZA = 0°, 5°, . . . , 85°. The fit is performed over the 4622 earth-atmosphere conditions. These NB-to-BB conversions are dependent only on the VZA and are not dependent on the surface type or the cloudiness. Table 1 provides the coefficients $\{a_i\}$ and $\{b_i\}$ for the GERB-2 instrument, and the residual root-mean-square (RMS) error of the fit. To avoid overfitting the data when Eqs. (11) and (12) are fit on the simulations, the SEVIRI NB radiances $L_{6,2}, \dots, L_{13,4}$ are randomly modified with a random noise having Gaussian distribution with a standard deviation equal to 5% of the average radiance in the channel. The RMS error associated with these NB-to-BB regressions is about $0.5 \text{ W m}^{-2} \text{sr}^{-1}$ (0.7%).

Before fitting Eqs. (11) and (12) on the simulations, the NB radiances $\{L_{\text{ch}}\}$ are randomly modified with a random noise having Gaussian distribution with a standard deviation equal to 5% of the average radiance in the channel. This is necessary to avoid the fits exploiting excessively slight correlations between the SEVIRI channels (overfitting the data). The 5% value is conservative limit for the calibration accuracy of the SEVIRI thermal channels Schmetz et al. 2002).

b. Solar contamination

The small contribution of reflected sunlight observed within the GERB longwave filter $L_{\text{lw,soi}}$ must be estimated. For this, a database of radiative transfer com-

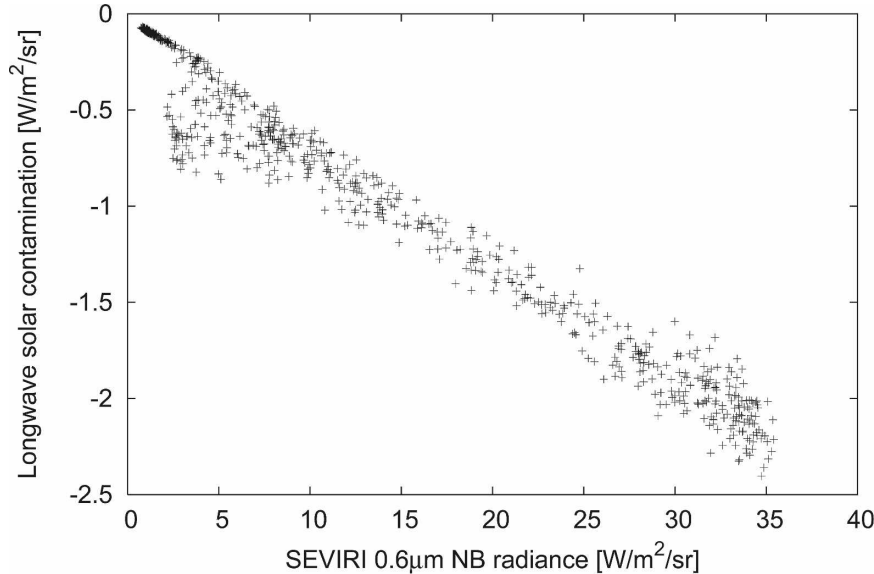


FIG. 2. Scatterplot of the contamination of reflected sunlight in the GERB-2 LW channel $L_{lw,sol}$ according to the SEVIRI 0.6- μm channel radiance. The dots represent the SBDART solar simulations at sun–earth–satellite geometry $\text{SZA} = 0^\circ$, $\text{VZA} = 50^\circ$, and $\text{RAA} = 90^\circ$.

putations in the solar part of the spectrum is used. The database contains simulations for 750 realistic earth–atmosphere conditions as described in Part I. Figure 2 gives an illustration of this contamination with respect to the 0.6- μm radiance for the geometry $\text{SZA} = 0^\circ$, $\text{VZA} = 50^\circ$, and $\text{RAA} = 90^\circ$, where SZA is the solar

zenith angle and RAA is the relative azimuth angle (0° in the forward direction). For these simulated spectra, the contamination always presents negative values.

This contribution is estimated as a second-order regression on the three visible channel radiances of the SEVIRI instrument at 0.6, 0.8, and 1.6 μm :

$$L'_{lw,sol} = c_0 + c_1L_{0.6} + c_2L_{0.8} + c_3L_{1.6} + c_4L_{0.6}^2 + c_5L_{0.8}L_{0.6} + c_6L_{0.8}^2 + c_7L_{1.6}L_{0.6} + c_8L_{1.6}L_{0.8} + c_9L_{1.6}^2, \tag{13}$$

where the coefficients of the regression $\{c_i\}$ are dependent on the SZA . Table 2 provides the $\{c_i\}$ values at $\text{SZA} = 0^\circ, 10^\circ, \dots, 80^\circ$. Before fitting Eq. (14) on the database of simulations, the simulated NB radiances

are randomly modified by a Gaussian noise having a standard deviation equal to 5% of the average radiance in the channel. The performance of the regression is assessed in the next section.

TABLE 2. Regression parameters $\{c_i\}$ used to estimate the solar contamination in the GERB-2 LW channel.

SZA	c_0	c_1	c_2	c_3	c_4	c_5	c_6	c_7	c_8	c_9	RMS W $\text{m}^{-2} \text{sr}^{-1}$
0°	-0.040 92	-0.027 97	-0.056 08	-0.001 97	0.000 38	-0.000 77	0.000 12	-0.000 88	0.000 25	-0.000 18	0.046
10°	-0.037 27	-0.029 10	-0.055 30	-0.004 56	0.000 35	-0.000 50	-0.000 23	-0.001 39	0.001 45	-0.000 46	0.044
20°	-0.038 11	-0.030 02	-0.053 04	-0.008 36	0.000 38	-0.000 50	-0.000 34	-0.001 40	0.001 36	0.000 46	0.042
30°	-0.037 78	-0.030 25	-0.052 22	-0.008 88	0.000 43	-0.000 57	-0.000 44	-0.001 55	0.001 56	0.000 62	0.039
40°	-0.035 87	-0.030 97	-0.048 27	-0.019 49	0.000 58	-0.000 97	-0.000 36	-0.001 10	0.000 12	0.004 43	0.037
50°	-0.034 74	-0.030 71	-0.045 48	-0.034 31	0.000 78	-0.001 63	-0.000 02	-0.000 89	-0.001 77	0.012 17	0.034
60°	-0.028 93	-0.031 47	-0.046 87	-0.027 04	0.000 70	-0.001 40	-0.000 50	-0.000 42	0.001 99	0.003 30	0.033
70°	-0.018 66	-0.033 99	-0.041 76	-0.037 00	0.001 06	-0.001 11	-0.002 64	-0.002 88	0.007 08	0.006 05	0.022
80°	-0.011 12	-0.032 29	-0.044 82	-0.037 05	0.002 26	-0.007 97	0.003 71	0.006 20	-0.006 38	0.013 12	0.012

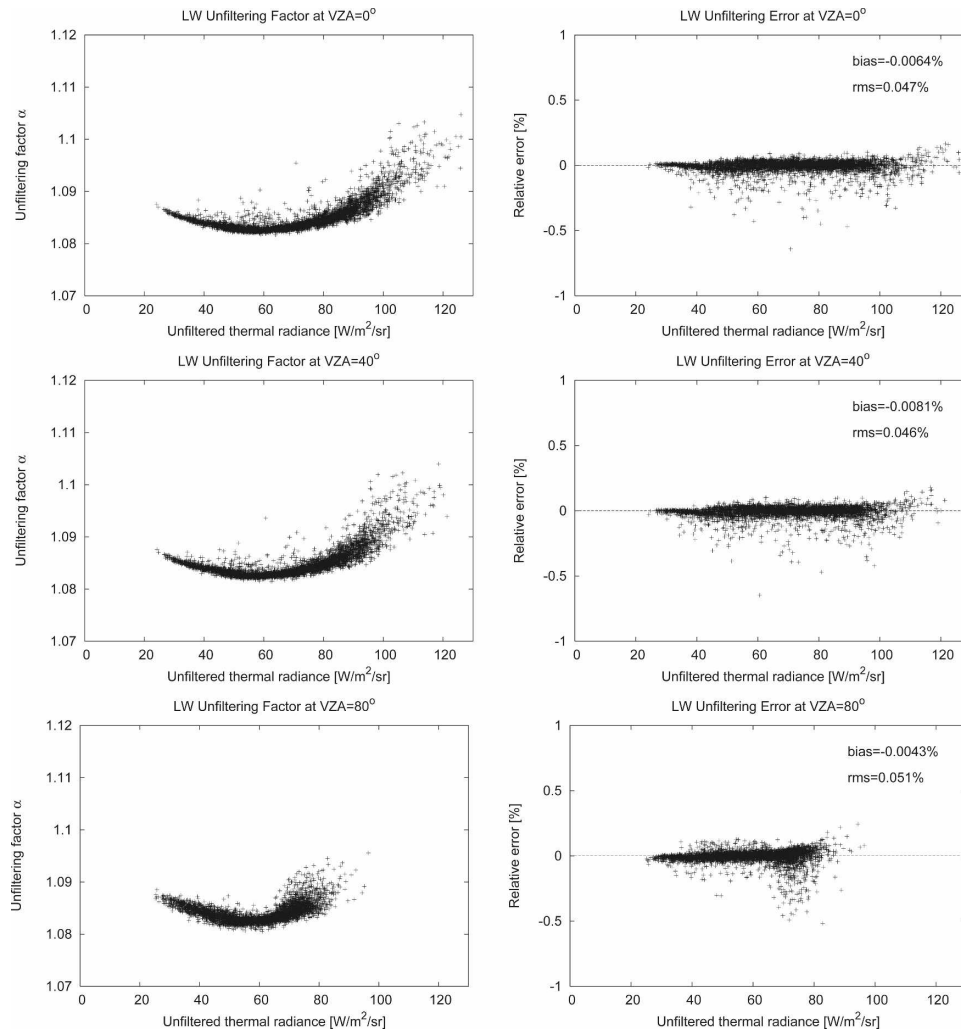


FIG. 3. (left) Theoretical unfiltering factor and (right) unfiltering error ϵ (%) for a viewing zenith angle of VZA = 0° , 40° , and 80° .

6. Theoretical assessment of unfiltering errors

In the following sections, the different sources of error that affect the unfiltering process are addressed using the radiative transfer simulations. All the errors are expressed as the difference between the estimated and the actual unfiltered radiances. So, positive (negative) error means that the unfiltering process overestimates (underestimates) the resulting BB unfiltered radiance.

a. Unfiltering regressions

Although the SEVIRI NB-to-BB theoretical regressions in Eqs. (11) and (12) are affected by an RMS error of about $0.45 \text{ W m}^{-2} \text{ sr}^{-1}$ or 0.7% (Table 1), the unfiltering error is expected to be much lower. This assumption must be verified on the database of simu-

lations. For each simulation $L_{\text{th}}(\lambda)$, the broadband radiances L_{th} and $L_{\text{lw,th}}$ and the narrowband radiances $L_{6,2}, L_{7,3}, \dots, L_{13,4}$ are computed with Eqs. (10). The unfiltering error for this simulated scene is then evaluated as

$$\epsilon(\%) = 100.0 \frac{L'_{\text{lw,th}} \frac{L'_{\text{th}}}{L'_{\text{lw,th}}} - L_{\text{th}}}{L_{\text{th}}}, \quad (14)$$

where L'_{th} and $L'_{\text{lw,th}}$ are the BB radiances estimated from the SEVIRI NB radiances through Eqs. (11) and (12). Figure 3 shows scatterplots of the unfiltering factor α_{lw} (left) and of the unfiltering error ϵ (right) versus L_{th} at three viewing zenith angles. Figure 3 also provides the unfiltering bias (the average of the unfiltering error) and RMS error:

TABLE 3. Unfiltering error according to scene type for the VZA = 0° simulations.

Scene type	$\langle L_{th} \rangle$ W m ⁻² sr ⁻¹	Bias W m ⁻² sr ⁻¹ (%)	RMS W m ⁻² sr ⁻¹ (%)
Clear sky	81.3	-0.0009 (-0.0011)	0.0343 (0.0422)
Cumulus	78.8	-0.0106 (-0.0134)	0.0452 (0.0574)
Stratocumulus	73.8	0.0103 (0.0140)	0.0300 (0.0407)
Stratus	72.3	0.0174 (0.0240)	0.0209 (0.0288)
Alto cumulus	70.6	-0.0265 (-0.0375)	0.0549 (0.0778)
Altostratus	60.4	0.0022 (0.0036)	0.0223 (0.0370)
Nimbostratus	59.4	0.0085 (0.0144)	0.0146 (0.0245)
Cirrus	57.1	-0.0456 (-0.0798)	0.0779 (0.1366)
Cirrostratus	43.3	-0.0096 (-0.0223)	0.0237 (0.0547)
Deep convection	41.5	-0.0013 (-0.0031)	0.0095 (0.0230)

$$\text{bias} = \frac{1}{N} \sum_{i=1}^N \epsilon_i, \quad (15)$$

$$\text{rms} = \sqrt{\frac{1}{N} \sum_{i=1}^N (\epsilon_i - \text{bias})^2}, \quad (16)$$

where the summation is done on the $N = 4622$ simulations. Figure 3 shows that the unfiltering does not introduce significant error. The RMS error of the unfiltering process is about 0.05%. However, an unfiltering error of up to approximately -0.5% (i.e., an underestimation) is observed for some cloud conditions. Table 3 gives the unfiltering error according to the ISCCP cloud classification. The largest error is observed for high and semitransparent (cirrus) clouds. However, even in this case the bias and the RMS errors remain very small (bias < 0.05 W m⁻² sr⁻¹ and RMS < 0.08 W m⁻² sr⁻¹).

b. Estimation of the solar contamination

The RMS error on the estimated solar contamination in the GERB-2 SW channel is estimated from the database of solar simulations. Figure 4 shows the scatterplot of the error ($L'_{lw,sol} - L_{lw,sol}$) according to the L_{sol} for the SZA = 0°, VZA = 50°, RAA = 90° geometry. The error can reach up to ±0.2 W m⁻² sr⁻¹ for reflective scene simulations. The RMS of this error is 0.046 W m⁻² sr⁻¹, which is, surprisingly, the same order of magnitude as the LW unfiltering error.

In general, the contamination is slightly overestimated for the cloudy scenes. As the contamination is subtracted, this leads to a small underestimation of the unfiltered thermal radiance. For the reflective desert scenes, the opposite error is observed.

c. Subtraction of the solar contamination

As stated in section 3, the implementation of the edition 1 GERB data processing does not properly

compensate for the solar contamination in the GERB LW measurement. This introduces a small error ϵ , which is the difference between Eqs. (8) and (9):

$$\epsilon = L'_{th} \frac{L_{lw}}{L'_{lw,th} + L'_{lw,sol}} - L'_{th} \frac{L_{lw} - L'_{lw,sol}}{L'_{lw,th}}. \quad (17)$$

Let $\beta_{lw} = L_{lw}/L'_{lw}$ be the ratio between the actual and NB-to-BB estimated longwave radiance. Equation (17) reduces to

$$\epsilon = L'_{th} (1 - \beta_{lw}) \frac{L'_{lw,sol}}{L'_{lw,th}}. \quad (18)$$

The largest errors are then expected for highly reflective scenes (i.e., high $L'_{lw,sol}$ values) for which the LW NB-to-BB regressions are inaccurate ($\beta_{lw} \neq 1$). Figure 5 shows the distribution of the error ϵ given by Eq. (18) evaluated on actual GERB and SEVIRI data from 1200 UTC 19 November 2006. On these data, errors up to 0.13 W m⁻² sr⁻¹ are observed. In average the error is 0.013 W m⁻² sr⁻¹, and the standard deviation is 0.016 W m⁻² sr⁻¹.

d. Sensitivity to SEVIRI absolute calibration

The impact of SEVIRI instrument absolute calibration on the GERB unfiltering must be assessed. The calibration of the SEVIRI thermal channels will impact the estimation of the unfiltering factor α_{lw} , while the calibration of the solar channel will affect the estimation of $L_{lw,sol}$. To assess this, the effects of changing the SEVIRI channel calibration by -5%, 0%, and +5% have been simulated.

For the unfiltering point of view, the worst case occurs when some thermal channels have a +5% change while others have -5% change. An overestimation of the GERB unfiltering factor by 0.09% is observed for -5% on 6.2-, 7.3-, 12-, and 13.4- μ m SEVIRI channels and +5% on 8.7-, 9.7-, and 10.8- μ m channels.

For the estimation of the reflected sunlight contamination via Eq. (14), the worst case is observed when the 0.6-, 0.8-, and 1.6- μ m SEVIRI channels are decreased by -5%. In this case, the estimate $L'_{lw,sol}$ is underestimated by 5%. As the sunlight contamination can reach up to -2.5 W m⁻² sr⁻¹ for very reflective scenes, the error on the unfiltered thermal radiance is $\epsilon = 0.14$ W m⁻² sr⁻¹. This is a small relative error for typical scenes ($L_{th} \sim 100$ W m⁻² sr⁻¹), but it can represent 0.5% of the signal for a very cold cloud ($L_{th} \sim 25$ W m⁻² sr⁻¹). The use of calibrated GERB shortwave observations could improve the estimate of the $L'_{lw,sol}$ contamination, but a constraint in the implementation of the data processing system prevents us from doing this.

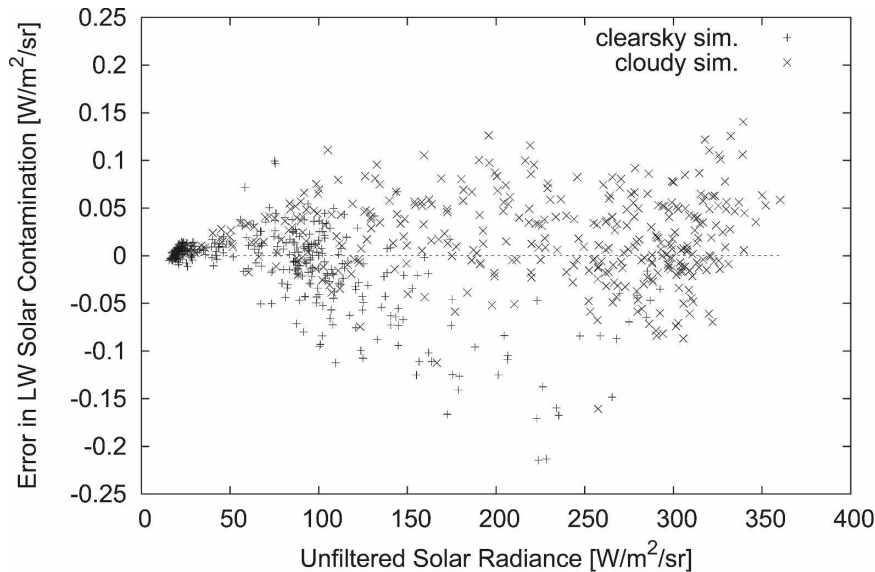


FIG. 4. Theoretical error in the estimation of the LW solar contamination for the SZA = 0° , VZA = 50° , and RAA = 90° simulations.

e. Mixed-scene pixels

The relation between the broadband radiance and unfiltering factor is highly nonlinear, as illustrated in Fig. 3. The clear-sky warm scenes and the very cold cloud scenes have higher unfiltering factor ($\alpha_{lw} \sim 1.087$) than the temperate cloudy scenes ($\alpha_{lw} \sim 1.082$ for $L_{th} \sim 60 \text{ W m}^{-2} \text{ sr}^{-1}$). So, in the hypothetical case of a footprint half covered by very cold cloud and half covered by warm clear-sky scene, the observed radiances will have a medium value and the unfiltering factor will be underestimated by up to 0.5%. For this reason, the GERB unfiltering is realized over boxes of 3×3 SEVIRI pixels instead of the instrument native footprint of 45 km. This approach is well suited for the GERB instrument, as the large GERB footprints may contain a mixture of scenes having different unfiltering factors.

We used SEVIRI data to evaluate the statistic of unfiltering factor at different spatial resolution ($3 \text{ km} \times 3 \text{ km}$, $9 \text{ km} \times 9 \text{ km}$, and $45 \text{ km} \times 45 \text{ km}$). As expected, the worst case was found to occur for mixed pixels. In this case, if the unfiltering was done at the 45-km GERB footprint resolution, the error would have reached 0.14%. For the same condition, the error is, however, negligible ($\epsilon \ll 0.03\%$) when the unfiltering is realized at the 10-km resolution.

f. Pixel-to-pixel variability

Each line in the GERB level 1.5 SW and TOT image is obtained with a distinct detector element. The LW

unfiltering implemented for edition 1 of the GERB level 2 products is based on the average spectral response defined by Eq. (3). We do not expect a significant difference in the spectral response of the detectors. The quantification of the error introduced by this assumption is not obvious. Indeed, the accuracy of the instrumental characterization of the spectral response at the detector element level is not sufficient. For the SW channel, the study (Mlynyczak et al. 2006) of the pixel-to-pixel variability by cross comparison with CERES radiance at the GERB detector level is an ongoing activity. It should also be noted that the current implementation of the ground processing software does

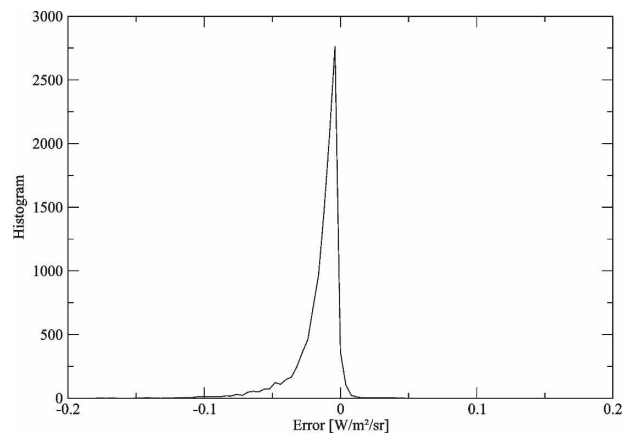


FIG. 5. Error introduced on the thermal radiance because of the incorrect subtraction of the solar contamination in the LW channel.

not allow a detector-level unfiltering. The LW radiances are indeed obtained from a spatial interpolation of the TOT channel images, and therefore cannot be associated with a single detector.

7. Intercomparison with the CERES unfiltered radiances

Cross comparisons between GERB edition 1 and CERES data have been made for two weeks in 2004 (21–27 June and 11–17 December). These periods have been selected as covering special observation campaigns when the CERES FM2 instrument has been operated in “GERB” scanning mode to optimize the number of coangular observations. The latest editions of the CERES Single Scanner Footprint (SSF) data for the FM2 and FM3 instruments have been used: edition 2B for FM2 and edition 1B for FM3.

For each GERB averaged rectified geolocated (ARG) pixel LW unfiltered radiance, the average corresponding CERES value within the pixel is evaluated by averaging all the CERES data with observation times within 170 s of the ARG time integration period and with angles between the GERB and CERES directions of observation smaller than 5° . The numbers of such collocated and coangular observations is 60 989 for the FM2 and 21 557 for the FM3. The value of the special GERB scanning mode employed by FM2 is obvious in the extra matches obtained with this instrument.

For the scene-type analysis, the ratio of the mean GERB and mean CERES LW unfiltered radiance is evaluated in bins of $10 \text{ W m}^{-2} \text{ sr}^{-1}$ of GERB unfiltered radiance. Figure 6 shows this ratio for the two CERES instruments and for day and night conditions. Within each GERB radiance bin, the uncertainties on the ratio is evaluated as $\pm 3/\sqrt{N}\sigma_{\text{ceres}}/\mu_{\text{ceres}}$, where N is the number of observations; and σ and μ_{ceres} are the standard deviation and the average values of the CERES distribution, respectively.

For FM3, the day and night ratios are very consistent. For FM2, higher GERB/CERES ratios are observed during the day than during the night. However, it is thought that this discrepancy is coming from the CERES side. Indeed, the FM2 instrument has been operated for a long time period in rotating azimuth plan (RAP) scanning mode, and this mode is known to accelerate the deposition of contaminant on the SW quartz filter. This results in a daytime underestimation of the CERES LW radiance that is going to be corrected in the future edition 3 data of the CERES dataset. The CERES team is currently working at the production of an edition 3 database that should remove most of the instrument spectral response ageing.

Figure 6 shows that the scene-type dependency is quite limited. The GERB/CERES ratio exhibits a minimum value for temperate scenes with radiances of $\sim 60 \text{ W m}^{-2} \text{ sr}^{-1}$. This minimum value probably results from the fact that the theoretical errors in the GERB and CERES unfiltering have opposite signs for cloudy scenes. The CERES LW radiances are expected to be slightly overestimated for cloudy scenes (Loeb et al. 2001), while GERB is expected to underestimate the radiance over high semitransparent clouds (see Fig. 3 and Table 3). Higher relative uncertainty affects the intercomparison for the coldest bins (high-level clouds with $L < 50 \text{ W m}^{-2} \text{ sr}^{-1}$). The FM2 intercomparison indicates, however, a good absolute agreement in this case.

All scenes together, the GERB/CERES ratios are 0.993 ± 0.001 for the FM2 and 0.982 ± 0.002 for the FM3.

8. Summary

The new GERB instruments measure SW and TOT filtered radiances that must be converted to unfiltered reflected solar and emitted thermal radiances—and later corresponding fluxes—for scientific usages. The unfiltering method for the GERB-2 edition 1 synthetic longwave channel is presented. The method takes advantage of the spectral information available from the SEVIRI multispectral weather imager that is on the same satellite platform. The unfiltering is realized through a set of regressions that links the unfiltering factor to the NB thermal channels of SEVIRI. The regressions' coefficients are derived from a large database of radiative transfer computations. The theoretical error analysis shows that the instantaneous unfiltering error is always small, with an RMS error of about 0.05%. A larger unfiltering error is observed for some kinds of cloudiness, for instance, up to 0.08% RMS error for cirrus cloud. During the daytime, the solar contamination in the LW channel is estimated with a regression on the SEVIRI visible channel radiances. The RMS error on this estimate is also low, having the same magnitude as the unfiltering error. The uncertainty introduced on the unfiltered radiance is the sum of these two contributions.

The impact of the SEVIRI channel absolute calibration is assessed assuming a 5% uncertainty on the NB measurements of the SEVIRI instrument. In the worst case, this uncertainty introduces an error of $0.26 \text{ W m}^{-2} \text{ sr}^{-1}$ on the GERB unfiltered thermal radiance. Half of this error comes from the estimation of the solar contamination and half from the unfiltering itself.

The intercomparisons with CERES observations

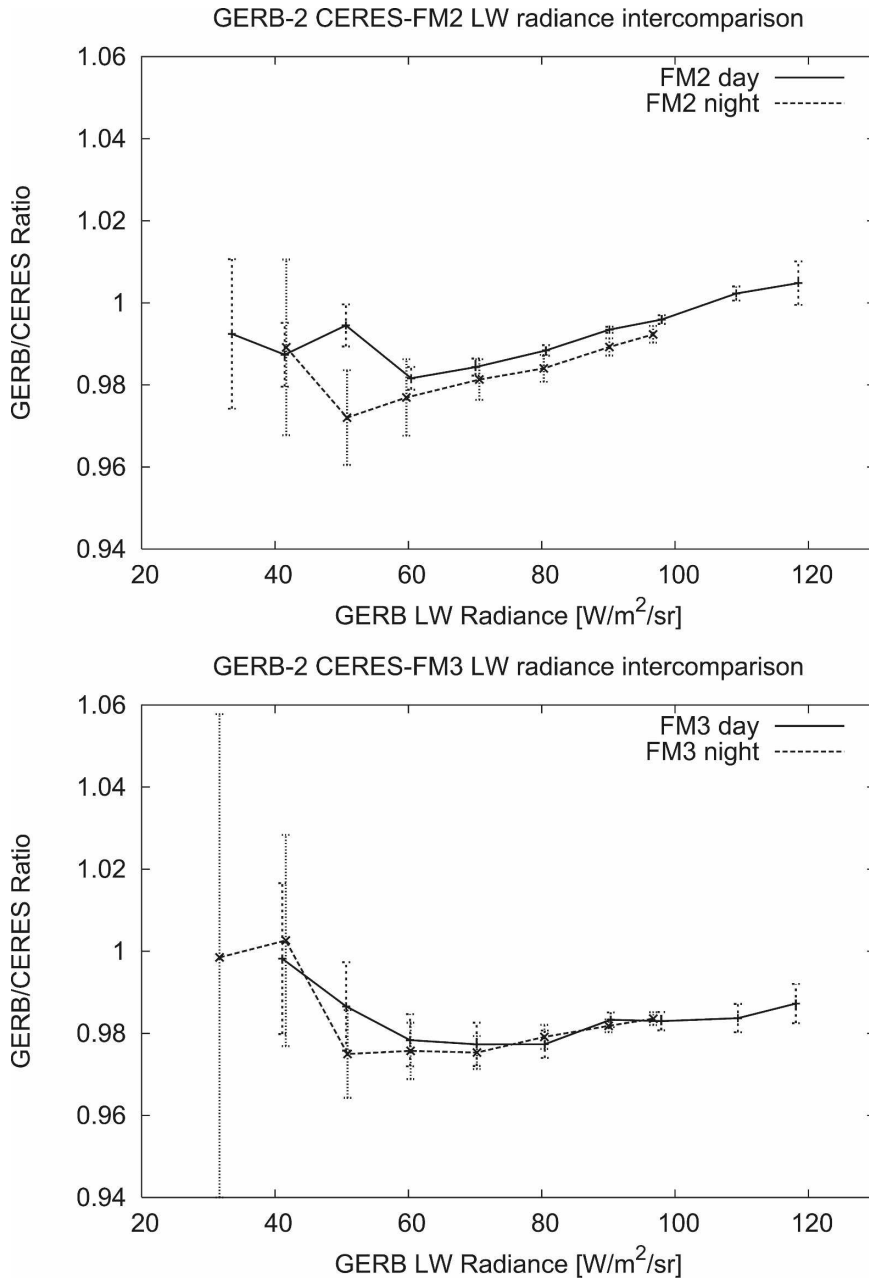


FIG. 6. GERB/CERES LW unfiltered radiance ratio for (top) FM2 and (bottom) FM3.

provide additional confidence in the unfiltering and on the absolute calibration of both instruments. All scenes together, GERB unfiltered radiances are lower than CERES by 0.7% for FM2 and 1.8% for FM3. The agreement is good for FM2, while for FM3 it is just out of the cumulated calibration uncertainties objectives, which are 1% for GERB and 0.5% for CERES. The scene-dependent variation of the GERB/CERES ratio is explained by the unfiltering error of opposite sign for the two instruments' data for cloudy scenes.

In contrast to the solar reflected radiances (Part I), this evaluation of the emitted thermal radiances shows no evidence of significant error affecting either the GERB LW spectral response curve or the LW unfiltering and subtraction of the solar contamination.

Acknowledgments. The authors are grateful to the Atmospheric Sciences Data Center at NASA Langley Research Center for providing the CERES data used in this study.

REFERENCES

- Chevallier, F., A. Chédin, F. Chéruy, and J. J. Morcrette, 2000: TIGR-like atmospheric-profile databases for accurate radiative-flux computation. *Quart. J. Roy. Meteor. Soc.*, **126**, 777–785.
- Clerbaux, N., S. Dewitte, L. Gonzalez, C. Bertrand, B. Nicula, and A. Ipe, 2003: Outgoing longwave flux estimation: Improvement of angular modelling using spectral information. *Remote Sens. Environ.*, **85**, 389–395.
- , and Coauthors, 2008: Unfiltering of the Geostationary Earth Radiation Budget (GERB) data. Part I: Shortwave radiation. *J. Atmos. Oceanic Technol.*, **25**, 1087–1105.
- Dewitte, S., L. Gonzalez, N. Clerbaux, A. Ipe, and C. Bertrand, 2008: The geostationary earth radiation budget edition 1 data processing algorithms. *Adv. Space Res.*, **41**, 1906–1913.
- Harries, J. E., and Coauthors, 2005: The Geostationary Earth Radiation Budget Project. *Bull. Amer. Meteor. Soc.*, **86**, 945–960.
- Loeb, N., K. Priestley, D. Kratz, E. Geier, R. Green, B. Wielicki, P. Hinton, and S. Nolan, 2001: Determination of unfiltered radiances from the Clouds and the Earth's Radiant Energy System instrument. *J. Appl. Meteor.*, **40**, 822–835.
- Mlynczak, P., G. Smith, P. Szweczy, J. Russell, H. Harries, S. Dewitte, and N. Clerbaux, 2006: Comparisons of GERB and CERES measurements. Preprints, *12th Conf. on Atmospheric Radiation*, Madison, WI, Amer. Meteor. Soc., 13.1. [Available online at <http://ams.confex.com/ams/pdfpapers/111906.pdf>.]
- Ricchiazzi, P., S. Yang, C. Gautier, and D. Sowle, 1998: SBDART: A research and teaching software tool for plane-parallel radiative transfer in the earth's atmosphere. *Bull. Amer. Meteor. Soc.*, **79**, 2101–2114.
- Rosow, W., and R. Schiffer, 1991: ISCCP Cloud Data Products. *Bull. Amer. Meteor. Soc.*, **72**, 2–20.
- Schmetz, J., P. Pili, S. Tjemkes, D. Just, J. Kerkmann, S. Rota, and A. Ratier, 2002: An introduction to Meteosat Second Generation (MSG). *Bull. Amer. Meteor. Soc.*, **83**, 977–992.
- Wielicki, B. A., B. R. Barkstrom, E. F. Harrison, R. B. Lee III, G. L. Smith, and J. E. Cooper, 1996: Clouds and the earth's radiant energy system (CERES): An earth observing system experiment. *Bull. Amer. Meteor. Soc.*, **77**, 853–868.